On the dynamics of flame edges in diffusion-flame/vortex interactions

Miguel Hermanns [a], Marcos Vera [b,*], Amable Liñán [a]

1. Introduction

Often in applications, the characteristic scales associated with the combustion processes are smaller than the smallest scales of the turbulence. Combustion occurs in the form of laminar flames embedded in thin mixing layers that are locally distorted and strained by vortices of different scales [1]. Thus, flame/vortex interaction is a topic of major importance for the understanding of fundamental combustion processes involving the coupling between fluid dynamics and combustion, such as turbulent combustion and combustion instability [2].

Aspects of the interaction of single vortices with reacting mixing layers—or diffusion flames—have been studied analytically by several authors [3–6]. These analyses aimed to describe the flame structure, the global enhancement of the chemical reaction due to the vortex roll-up, and the structure of the burned core.

The interaction of vortices with flames has also been studied in different configurations both numer-

ically [7–10] and experimentally [11]. In particular, the head-on interaction of a vortex pair or vortex ring with a laminar flame is a canonical configuration that has received great attention in the past years [12–17]. This kind of interaction provides relevant information such as the time evolution of the flame front and the flame structure, as well as information on extinction limits, pocket formation, effects of vortex size and strength, etc. Numerical and experimental studies of local flame extinction in flame/vortex interactions [18–20] also lead to improved definitions of the different regimes in turbulent combustion diagrams, which summarize the current knowledge in the field [21,22].

There is also strong evidence from theoretical [23,24], numerical [25–28], and experimental [29–35] work that triple flames, or the more general flame edges, play an important role in the dynamics of locally extinguished regions in turbulent diffusion flames [36]. Local flame extinction leads to the formation of flame holes (chemically frozen regions of low temperature where the reactants mix without chemical reaction) which are separated by flame edges, typically in the form of thin premixed flames, with rich and lean branches, from regions of near equilibrium flow, where the reactants only coexist in a thin diffusion flame.

In a turbulent flow field the local strain rate experienced by the flame is a random variable, so that turbulent diffusion flames typically exhibit a random distribution of extinguished holes. But as soon as the strain rate decreases below the critical value in the vicinity of these holes, they may be reignited by the surrounding flame elements, which may propagate toward the fresh mixture in the form of triple or edge flames [37]. In this context, flame/vortex interactions constitute a well-defined system of intermediate complexity between steady laminar flames and turbulent ones, appropriate to investigate unsteady and curvature effects [38], as well as local flame extinction and reignition phenomena [27,39]. Such investigations appear as a necessary step toward the extension of the classical isolated flamelet models, which regard the turbulent diffusion flame locally as a steady, one-dimensional, laminar flame [1], into more involved interacting flamelet models accounting for local extinction/reignition events [40,41].

According to flamelet theory, the extinction and reignition behavior of a turbulent diffusion flame is determined by the local value of the Damköhler number, $\mathrm{Da} = (\delta_\mathrm{m}/\delta_\mathrm{L})^2$, defined in terms of the effective thickness, δ_m, of the mixing layer and the laminar flame thickness, $\delta_\mathrm{L} = D_\mathrm{T}/S_\mathrm{L}$, where S_L denotes the planar stoichiometric flame velocity and D_T is a characteristic thermal diffusivity of the system. The effective thickness of the mixing layer can be defined in terms of the instantaneous value $\chi_\mathrm{s} = D_\mathrm{T}|\nabla Z|_\mathrm{s}^2$ of the scalar dissipation rate at the stoichiometric surface, namely $\delta_\mathrm{m} = (D_\mathrm{T}/\chi_\mathrm{s})^{1/2}$. Accordingly, the local Damköhler number, which can also be written as $1/(\chi_\mathrm{s} t_\mathrm{L})$, represents the ratio of the characteristic diffusion time, $1/\chi_\mathrm{s} = \delta_\mathrm{m}^2/D_\mathrm{T}$, to the characteristic chemical time, $t_\mathrm{L} = \delta_\mathrm{L}^2/D_\mathrm{T}$, defined here as the residence time in the preheat zone of the stoichiometric premixed flame [42].

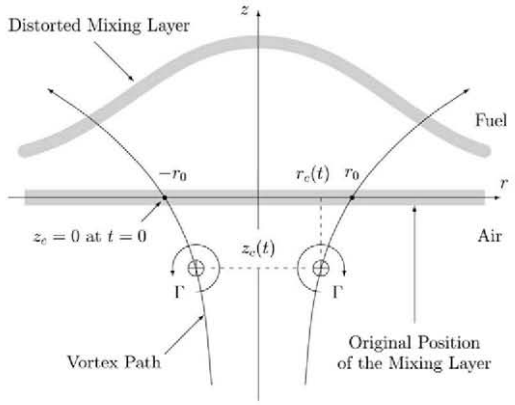

Fig. 1. Sketch of a distorted mixing layer perturbed by a vortex ring.

The aim of this paper is to describe the dynamics of the triple flames, or flame edges, that appear after the local extinction by a laminar vortex ring of a diffusion flame established between two counterflowing gaseous fuel and air streams of the same density, a configuration sketched in Fig. 1. The flame will be locally quenched when the flame/vortex interaction stretches the distorted diffusion flame with a nondimensional stretch rate $\chi_\mathrm{s}\delta_\mathrm{L}/S_\mathrm{L} = (\delta_\mathrm{L}/\delta_\mathrm{m})^2$ ($\equiv 1/\mathrm{Da}$) above a critical value of order unity, or, equivalently, when the Damköhler number, Da, diminishes below a critical extinction value, herein denoted as $\mathrm{Da_e}$ [43], determined by the details of the chemistry.

As previously discussed, the local extinction of the flame leads to the formation of flame holes (or annulus), where both reactants mix without reaction. Such holes are separated from the diffusion flame by flame edges that can propagate in either direction—as ignition fronts or failure waves—depending on the local flow conditions [24]. Hereafter, the front propagation velocity (relative to the upstream flow) will be denoted by U_F. These flame edges constitute transition structures that join the near-equilibrium and nearly frozen solutions of the S-shaped curve characterizing the response of nonpremixed flames. Thus, for values of the Damköhler number larger than a critical value, $\mathrm{Da} > \mathrm{Da}^*$ ($>\mathrm{Da_e}$), the flame edges propagate along the stoichiometric surface toward the unburned mixture as ignition fronts (triple or edge flames with positive velocity, $U_\mathrm{F} > 0$, relative to the upstream flow),

while for $Da^* > Da$ ($>Da_e$) they behave as failure waves (edge flames with negative velocity, $U_F < 0$) that recede from the unburned mixture. The analysis of the scalar dissipation rate at the stoichiometric surface, which yields the local value of Da at the flame front, is therefore of interest for the description of the evolution of extinguished holes [44]. After local flame extinction, the holes grow rapidly in size if the stretch rate is maintained, because close to the extinction value of Da, of order unity, the dimensionless edge front velocity U_F/S_L is negative and, more importantly, the flame-edge displacement is soon assisted by the flow velocity components associated with the stretch. The hole collapse will occur only when the stretch rate is decreased again [17].

This paper represents an extension of the previous work by Vera and Liñán [45] (herein referred to as VL) on the unsteady response of reacting mixing layers (or diffusion flames) perturbed by vortices. For the sake of brevity, in this sequel paper we will focus our attention on axisymmetric flame/vortex interactions, which are the configuration typically found in the experimental literature. Moreover, axisymmetric interactions exhibit much richer dynamics than their two-dimensional counterpart, as demonstrated by the existence of off-axis (i.e., annular) extinction patterns in certain regimes [34], a phenomenon much less probable to observe in two-dimensional interactions. As in VL, the analysis presented here is confined to the near-stagnation point region, where the strain rate of the unperturbed velocity field, A_0, is constant, and is restricted to cases where the typical vortex ring radius, r_0, is large compared to both the size, δ_v, of the vorticity core and the characteristic thickness, $(D_T/\chi_{s,0})^{1/2}$, of the unperturbed mixing layer, defined in terms of the unperturbed value $\chi_{s,0} \sim A_0$ of the scalar dissipation rate at the stoichiometric surface. Emerging as an important process in the physical model, the dynamics of the flame edges is modeled based on previous numerical results, with heat release effects fully taken into account, that provide the propagation velocity of triple and edge flames in mixing layers in terms of the local Damköhler number.

As in our previous work, our aim is not to develop a fully computational model to solve the problem, but to develop a theoretical framework, using asymptotic techniques and order of magnitude estimates, which may contribute to the understanding of the basic physical mechanisms that take part in flame/vortex interactions. As usual for theoretical considerations, several hypotheses must be introduced, the most restrictive of them being the assumption of constant density. However, as demonstrated from comparisons with a few selected experimental visualizations, many aspects of flame vortex interactions are still well reproduced.

This is specially true in the most interesting limit of strong vortices interacting with robust flames, when the large convective velocities imposed by the vortex dominate over both the transversal displacement velocities induced by thermal expansion at the reacting mixing layer and the flame-edge propagation velocity along the stoichiometric surface, which otherwise determine the evolution of the flame sheet during the interaction.

The paper is organized as follows. We begin in Section 2 with the description of the velocity field. In Section 3 we describe the evolution of the stoichiometric surface, introducing the criterium for local flame extinction. In Section 4 we discuss flame element tracking and dynamics, and the most interesting range of parameters is identified using order of magnitude estimates. The numerical method is described in Section 5, and after choosing five representative cases from the experimental literature, the numerical results are discussed and validated in Section 6. Finally, the concluding remarks are presented in Section 7.

2. Description of the velocity field

In this section we introduce the velocity field that describes the perturbations introduced by a vortex ring (in an axisymmetric configuration) in the mixing layer in the stagnation region between two gaseous counterflowing streams of fuel and air. We consider a three-dimensional incompressible axisymmetric configuration, and adopt a cylindrical coordinate system (r, θ, z) with its origin at the stagnation point of the unperturbed mixing layer and the z-axis pointing toward the fuel side, as shown schematically in Fig. 1.

When the fuel and oxidizer streams have the same density, the unperturbed potential velocity field near the stagnation point is given by $u = A_0 r/2$ and $v = -A_0 z$, where the coordinates r and z are tangential and transverse to the unperturbed mixing layer respectively, and u and v are the corresponding velocity components along the r- and z-axes. As done in VL, this velocity field has to be modified to account for the unsteady perturbations induced by the vortex ring.

In order to characterize the strength and size of the vortex, we shall use the vortex circulation Γ and the value r_0 of the vortex ring radius at the time of crossing of the vortex through the original plane $z = 0$ of the mixing layer. Without loss of generality, we shall assume that the vortex ring is coaxial with the basic flow. Then, if the Reynolds numbers Γ/ν, where ν is the kinematic viscosity of the fluid, and $r_0^2 A_0/\nu$ are sufficiently large compared to unity, as we shall assume here, the axisymmetric velocity field

associated with the vortex ring can be added to the unperturbed straining field to obtain the instantaneous velocity field

$$\tilde{u} = \frac{\xi}{2} + \frac{\widetilde{\Gamma}}{\pi \xi_c}\left(\frac{\xi_c}{2\xi}\right)^{3/2}\left(\frac{\eta - \eta_c}{\xi_c}\right) I_1(\mu), \tag{1a}$$

$$\tilde{v} = -\eta - \frac{\widetilde{\Gamma}}{\pi \xi_c}\left(\frac{\xi_c}{2\xi}\right)^{3/2}\left[\frac{\xi}{\xi_c} I_1(\mu) - I_0(\mu)\right], \tag{1b}$$

where $\mu = [(\eta - \eta_c)^2 + (\xi - \xi_c)^2]/(2\xi\xi_c)$, and the integrals $I_0(\mu)$ and $I_1(\mu)$ can be expressed in terms of complete elliptic integrals of the first and the second kind (see VL for details). As previously discussed, in the above expressions we use as characteristic length the radius r_0 of the vortex ring at the time it crosses the plane of the original mixing layer, choose the crossing time as time origin, and use A_0^{-1} and $A_0 r_0$ as characteristic time and velocity scales to define the dimensionless coordinates $\xi = r/r_0$ and $\eta = z/r_0$, time $\tau = A_0 t$, and velocities $\tilde{u} = u/(A_0 r_0)$ and $\tilde{v} = v/(A_0 r_0)$.

The axisymmetric motion of the vortex ring, of dimensionless core position $r_c/r_0 = \xi_c$ and $z_c/r_0 = \eta_c$, results from the superposition of the velocity due to the baseline strain A_0 and the self-induced velocity V_I by the vortex ring, which, assuming a Gaussian vorticity distribution with a vortex core thickness of size $\delta_v \ll r_c$, can be written as $[\Gamma/(4\pi r_c)][\log(8r_c/\delta_v) - 0.558]$. Then the vortex core position is given as a function of time by

$$\xi_c = e^{\tau/2},$$

$$\eta_c = \widetilde{\Gamma}\left[\left(2\alpha_0 - \frac{1}{\pi} + \frac{\tau}{2\pi}\right)e^{-\tau/2} - \left(2\alpha_0 - \frac{1}{\pi}\right)e^{-\tau}\right], \tag{2}$$

where

$$\widetilde{\Gamma} = \frac{\Gamma}{2r_0^2 A_0} \tag{3}$$

is the nondimensional vortex strength, and α_0 represents the dimensionless self-induced velocity V_{I0} of the vortex ring at $\tau = 0$, namely

$$\alpha_0 = \frac{V_{I0}}{(\Gamma/2r_0)} = \frac{1}{2\pi}\left[\log\left(\frac{8\mathrm{Pe}_0}{\mathrm{Pr}}\right)^{1/2} - 0.558\right]. \tag{4}$$

Here $\mathrm{Pr} = \nu/D_T \equiv 0.72$ is the Prandtl number, assumed to be constant, and

$$\mathrm{Pe}_0 = \frac{r_0^2 A_0}{D_T} \tag{5}$$

is the Peclet number of the unperturbed flow, considered to be large but finite. It is important to note that in the derivation of Eq. (2) we have considered that the evolution of the (Gaussian) vorticity core is such that its core size, δ_v, is constant as a result of the radial competition between inward convection and outward diffusion, namely

$$\delta_v = \left(\frac{8\nu}{A_0}\right)^{1/2} \tag{6}$$

(see the Appendix in VL for details). Note also that, unlike in VL, in the present work the vortex ring propagates upward, which allows us to match the experimental configurations found in the literature [15,31,34].

As can be seen from Eqs. (1)–(4), the main nondimensional parameters characterizing the velocity field are the nondimensional vortex strength, $\widetilde{\Gamma}$, and the Peclet number of the unperturbed flow, Pe_0. It should be noted that the dimensionless self-induced velocity of the vortex ring, α_0, given by Eq. (4) in terms of the Peclet and Prandtl numbers is not a free parameter.

The interaction between the vortices and the mixing layer is much more complex in the more general case of counterflowing streams with different densities [46,47], which is not treated here. In this case vorticity is generated at the interface by baroclinic effects, which affects strongly the dynamics of the vortices and the interface distortion. This, in turn, modifies the local values of the strain rate, whose time evolution ultimately determines the flame response. However, the assumption made here that the fuel and oxidizer streams have the same density is not that far from conditions in experiments, where the fuel stream is strongly diluted with nitrogen, so that the density ratio ρ_F/ρ_{O_2} is close to one.

3. Flame-sheet evolution and local flame extinction

We shall consider a one-step overall reaction of the form

$$\mathrm{F} + s\mathrm{O}_2 \rightarrow (1+s)\mathrm{products} + (q), \tag{7}$$

where a mass s of oxygen is consumed and an amount q of heat is released per unit mass of fuel. In the Burke–Schumann limit the chemical reaction proceeds infinitely fast, so that fuel and oxidizer do not coexist. Their mass fractions Y_F and Y_{O_2} can be calculated, if we assume equal diffusivities of mass and heat, D_T, in terms of the mixture fraction

$$Z = \frac{SY_F/Y_{F0} - Y_{O_2}/Y_{O_20} + 1}{S+1}, \tag{8}$$

where Y_{F0} and Y_{O_20} are the mass fractions of fuel and oxygen at their corresponding feeding streams,

and $S = sY_{F0}/Y_{O_20}$ is the overall air-to-fuel mass stoichiometric ratio. Then Z is a conserved scalar of unit concentration in the fuel stream and zero concentration in the air stream.

If we assume, in addition, constant values for the gas density ρ and the thermal diffusivity D_T, the conservation equation for the mixture fraction Z can be written in nondimensional form as

$$\frac{\partial Z}{\partial \tau} + \mathbf{u}\cdot\nabla Z = \frac{1}{\mathrm{Pe}_0}\nabla^2 Z, \tag{9}$$

where the velocity field $\mathbf{u} = (\tilde{u}, \tilde{v})$ is given by Eqs. (1)–(4). The above equation has to be solved with the boundary conditions $Z = 0$ in the air stream, coming from $\eta = -\infty$, and $Z = 1$ in the fuel stream, coming from $\eta = \infty$. The initial condition at $-\tau \gg 1$ corresponds to the unperturbed planar mixing layer:

$$Z = Z_0(\eta) = 1 - \frac{1}{2}\mathrm{erfc}\left[(\mathrm{Pe}_0/2)^{1/2}\eta\right]. \tag{10}$$

Under the above assumptions, the flame sheet is located at the surface where Z takes its stoichiometric value, $Z_s = 1/(S+1)$, and the rate of fuel consumption per unit flame surface is determined by the value $|\nabla Z|_s$ of the mixture fraction gradient at the stoichiometric surface.

The diffusion flame will be locally quenched when the instantaneous value of the scalar dissipation rate at the stoichiometric surface, $\chi_s = D_T|\nabla Z|_s^2$, exceeds its critical extinction value, $\chi_{s,e}$, or, equivalently, when the Damköhler number diminishes below its critical extinction value, $\mathrm{Da}_e = 1/(\chi_{s,e}t_L)$ [43]. Accordingly, the ratio

$$\frac{\chi_{s,e}}{\chi_{s,0}} = \frac{\mathrm{Da}_0}{\mathrm{Da}_e} \equiv \mathcal{R} \tag{11}$$

of the critical scalar dissipation rate at extinction, $\chi_{s,e}$, to its unperturbed value, $\chi_{s,0}$, measures the *robustness* of the flame to flow perturbations, indicating how far from extinction the flame is in the unperturbed condition. Experimentally, the robustness parameter $\mathcal{R}$ can be varied independent of $\widetilde{\Gamma}$ and Pe_0 by changing the dilution of the fuel stream, which modifies the critical scalar dissipation rate at extinction.

The above discussion reveals the main nondimensional parameters that characterize the evolution of the flame sheet and the local flame extinction/reignition phenomena. These are the Peclet number of the unperturbed flow, Pe_0, the overall air-to-fuel stoichiometric ratio, S, and the robustness parameter, $\mathcal{R} > 1$. Remember that the Peclet number, Pe_0, together with the nondimensional vortex strength, $\widetilde{\Gamma}$, and the Prandtl number, Pr, determine also the flow field through Eqs. (1)–(4).

The above nondimensional parameters are closely related with two alternative relevant parameters, namely the Reynolds number of the vortex based on the vortex circulation [3],

$$\mathrm{Re}_\Gamma = \frac{\Gamma}{\nu} \sim \widetilde{\Gamma}\mathrm{Pe}_0, \tag{12}$$

which must be large for the vortices to maintain their identities during the interaction, and the overall Damköhler number of the interaction,

$$\mathrm{Da}_\Gamma = \frac{2r_0^2/\Gamma}{\delta_L/S_L} \sim \frac{\mathcal{R}}{\widetilde{\Gamma}}, \tag{13}$$

defined here as the ratio of the characteristic vortex turnover time, $t_T = 2r_0^2/\Gamma$, to the characteristic chemical time, $t_L = \delta_L^2/D_T$. Local flame extinction should be expected for $\mathrm{Da}_\Gamma \lesssim 1$.

It is worth noting that in the limit of strong vortices, $\widetilde{\Gamma} \gg 1$, the vortex ring will cross, without significant change in its structure, the original position of the mixing layer, displacing and wrapping it around the weakly distorted fluid surface that bounds the fluid moving with the vortex. In this relevant case, the roll-up of the flame sheet around the vortex introduces strong curvature effects and interactions between adjacent flame elements, processes that cannot be described using boundary layer approximations of the kind performed in VL. Therefore, for an accurate description of the structure of the mixing layer throughout the interaction, it is necessary to integrate Eq. (9) as is, without further simplifications.

A final remark will be made regarding the variable density effects due to the heat released at the flame. These effects cause a displacement of the outer flow, which is influenced by the pressure field generated by the vortex. These displacement velocities can be represented by a surface distribution of volume sources, that induces transverse displacement, which generates an irrotational perturbation flow to be added to the outer irrotational flow due to the baseline strain and the vortex ring.

This perturbation flow would be able to modify the vortex path if the displacement velocities were strong enough. However, this is not the case under the conditions considered here. Using order of magnitude estimates, it is easy to see that the ratio of the (viscous) transverse displacement velocities, $v_{dis} \sim (\nu A_T)^{1/2}$, being $A_T \sim V_{I0}/r_0 \sim \Gamma/r_0^2$ the characteristic strain induced by the vortex, to the characteristic velocity of the vortices, $v_T \sim r_0/t_T \sim \Gamma/r_0$, is of order

$$v_{dis}/v_T \sim (\nu/\Gamma)^{1/2}, \tag{14}$$

which is small when the Reynolds number Γ/ν is large. Therefore, consistent with the approximation of thin-cored vortices, which required the assumption $\Gamma/\nu \gg 1$, we may also neglect the effect of thermal expansion on the outer irrotational streams.

4. Flame-edge dynamics and flame element tracking

4.1. Flame-edge dynamics

As previously discussed, local flame extinction leads to the formation of flame edges that separate the burning and extinguished regions of the perturbed mixing layer. The dynamics of these edges is determined by the superposition of the velocity, $\mathbf{u}_s$, of the stoichiometric surface with respect to the laboratory reference frame and the flame-edge propagation velocity along the stoichiometric surface, U_F.

The velocity of a point located on the stoichiometric surface, $\mathbf{u}_s$, is due to the combined effect of convection and diffusion [48], namely

$$\mathbf{u}_s = \mathbf{u} + \mathbf{u}_d = \mathbf{u} - \frac{1}{\mathrm{Pe}_0}\frac{\nabla^2 Z}{|\nabla Z|}\mathbf{n} = \mathbf{u} - \frac{1}{\mathrm{Pe}_0}\left[k + \frac{\mathbf{n}\cdot\nabla(\mathbf{n}\cdot\nabla Z)}{|\nabla Z|}\right]\mathbf{n}, \tag{15}$$

where $\mathbf{u}$ is the convective velocity given in (1), and $\mathbf{u}_d$ is a diffusive velocity representing the effects of the curvature $k = \nabla\cdot\mathbf{n}$ and diffusion along the normal $\mathbf{n} = (\nabla Z/|\nabla Z|)_s$ (see Fig. 2 for details). The importance of the diffusive velocity $\mathbf{u}_d$ in practical cases has been recently demonstrated in numerical simulations of fully turbulent flows [28].

The propagation velocity of triple- and edge-flame fronts, U_F, measured with the planar stoichiometric flame velocity, S_L, is known to depend on the local Damköhler number, $\mathrm{Da} = 1/(\chi_s t_L)$, of the nonreacting mixing layer ahead of the triple flame, as well as on the overall air-to-fuel stoichiometric ratio S, the heat release parameter $\gamma = (T_e - T_0)/T_0$ defined in terms of the adiabatic flame temperature, T_e, and the temperature, T_0, of the feeding streams, and the Lewis numbers of the reactants [37], i.e.,

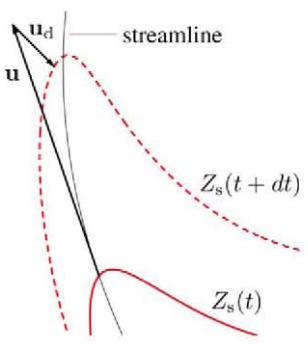

Fig. 2. The velocity of a discrete flame element, $\mathbf{u}_s$, results from the superposition of the convective velocity imposed by the flow, $\mathbf{u}$, and the diffusive velocity, $\mathbf{u}_d$, combining the effects of curvature and diffusion along the normal.

$$\frac{U_F}{S_L} = f(\mathrm{Da}, S, \gamma, \mathrm{Le}_i). \tag{16}$$

For a given composition of the feeding streams, the values of S, γ, and Le_i are known, and the dependence of U_F/S_L on Da can be determined numerically as done by Daou and Liñán [49] for constant-density flame edges in the symmetric configuration, $S = 1$.

Due to the absence of published results for more realistic cases, including heat release effects and nonsymmetric flames, here we have chosen to model the dependence of U_F/S_L on Da using an approximate analytic expression, in the spirit of previous work by Pantano and Pullin [50]. Although the curve $U_F/S_L = f(\mathrm{Da})$ could be determined numerically for realistic cases following a procedure similar to that described in [51], in the limit of strong vortices that we consider here the precise shape of this curve is not critical, since the convection velocity imposed by the vortex ring is typically large compared to the edge propagation velocity along the stoichiometric surface, $|\mathbf{u}_s| \gg U_F$, and therefore the exact shape of the curve $U_F/S_L = f(\mathrm{Da})$ is anticipated to have little impact on the numerical results.

In particular, we shall model the dependence of the front propagation velocity with the Damköhler number using the correlating expression

$$\frac{U_F/S_L}{(U_F/S_L)_\infty} = f(\Delta) = \begin{cases} 1 - a\Delta^{-1/2} \\ \quad \text{for } \tilde{\Delta} < \Delta < \infty, \\ 1 - a\tilde{\Delta}^{-1/2} + b\log\frac{\Delta-1}{\tilde{\Delta}-1} \\ \quad \text{for } 1 < \Delta < \tilde{\Delta}, \end{cases} \tag{17}$$

where $\Delta = \mathrm{Da}/\mathrm{Da}_e$ denotes the Damköhler number normalized with its extinction value Da_e, a and $\tilde{\Delta}$ are adjustable parameters, and we must choose $b = a(\tilde{\Delta} - 1)/(2\tilde{\Delta}^{3/2})$ to ensure the continuity of f and f' at $\Delta = \tilde{\Delta}$. It should be noted that even though Da_e does not appear explicitly in (17), it cannot be eliminated from the model, as can be seen from Eq. (21) below. Therefore, the order unity value of Da_e, which depends on the thermochemical parameters of the flame, S and γ, and on the details of the chemistry, emerges in principle as an additional parameter of our formulation. But the small sensitivity of the model to the precise value of Da_e allows us to set $\mathrm{Da}_e = 1$ for simplicity.

It is well known that the normalized front velocity $U_F/S_L \to -\infty$ as the Damköhler number approaches its extinction value, a condition that has been taken into account in modeling the behavior of $f(\Delta)$ as $\Delta \to 1$ in Eq. (17). On the other hand, the numerical values of U_F/S_L obtained for large (but finite) values of the Damköhler number can be fitted by assuming

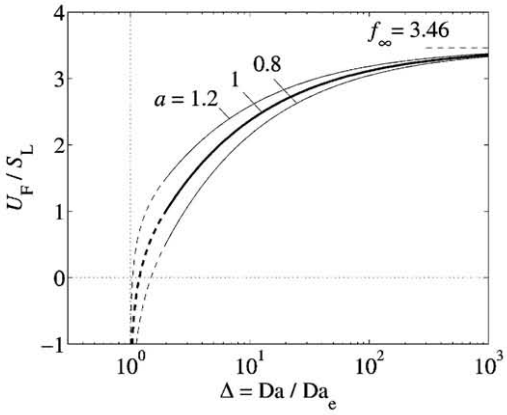

Fig. 3. Variation of the nondimensional front propagation velocity, U_F/S_L, with the normalized Damköhler number, $\Delta = \mathrm{Da}/\mathrm{Da_e}$, given by the flame-edge velocity model (17) for $f_\infty = 3.46$, $\tilde{\Delta} = 2$, and different values of a.

the asymptotic behavior $U_F/S_L \simeq (U_F/S_L)_\infty(1 - a\Delta^{-1/2})$ as $\Delta \to \infty$, first established by Daou and Liñán [49] and recently used by Fernández-Tarrazo et al. [51] to correlate numerical results accounting for heat release effects. Thus, for sufficiently large values of Δ the velocity becomes weakly dependent on the Damköhler number, growing to an asymptotic value $f_\infty = (U_F/S_L)_\infty$ for large Δ, which, due to thermal expansion effects in the flame front region, is larger than unity, typically of order 3 [25,51].

Here we shall use the value $f_\infty = 3.46$ taken from [51], which corresponds to undiluted methane–air flames. However, we can anticipate that the results presented here will be valid for other fuels, having values of γ (and thus of f_∞) close to that of methane. As an example, recent numerical simulations of flame edges in diluted hydrogen–air counterflow mixing layers give nondimensional propagation velocities very close to the value 3.46 considered here [52]. Fig. 3 shows the resulting model flame-edge velocity as a function of Δ for different values of a and $\tilde{\Delta} = 2$. As can be seen, the front propagation velocity decreases as a increases, hence this adjustable parameter plays a role similar to the Lewis number. The effect of $\tilde{\Delta}$ is negligible in the range $2 \lesssim \tilde{\Delta} \lesssim 5$. Thus, for definiteness here we shall use the curve corresponding to $a = 1$ and $\tilde{\Delta} = 2$, shown in thick lines in Fig. 3.

Once we have specified the functional dependence of U_F on Da, required to close the problem, the procedure that allows us to simulate the dynamics of the flame edges is as follows. The integration of Eq. (9) with the velocity field given by Eqs. (1)–(4) provides the time evolution of the perturbed mixing layer, which allows us to calculate the time evolution of the stoichiometric surface, $Z = Z_s$, as well as the stoichiometric value of the scalar dissipation rate, χ_s. From this, using Eq. (11), we can write the normalized Damköhler number appearing in (17) as

$$\Delta = \frac{\mathrm{Da}}{\mathrm{Da_e}} = \frac{\chi_{s,e}/\chi_{s,0}}{\chi_s/\chi_{s,0}} = \frac{\mathcal{R}}{\chi_s/\chi_{s,0}}, \tag{18}$$

where $\chi_{s,0} = D_T \mathrm{Pe}_0 \exp(-\mathrm{Pe}_0 \eta_{s,0}^2)/(2\pi r_0^2)$ is the unperturbed value of the scalar dissipation rate at the stoichiometric surface, located at $\eta = \eta_{s,0} = (2/\mathrm{Pe}_0)^{1/2}\mathrm{erfc}^{-1}[2(1-Z_s)]$. Using Eq. (18) together with Eq. (17), we can evaluate the front propagation velocity in terms of the normalized scalar dissipation rate. This, together with Eq. (15), determines the flame-edge dynamics.

As a final remark, it is worth noting that although the flame-edge propagation velocities implemented in our model include the effects of heat release through the parameter $f_\infty \sim 3$, the flame-edge velocity model (17) is only strictly valid for two-dimensional adiabatic flames. In particular, it does not show the effect of possible flame-edge interactions prior to flame-edge merging or the focusing/defocusing effect of hole curvature in the plane of the stoichiometric surface during the final stage of flame hole/disk collapse, which is known to increase substantially the front velocity [53,54] in these final stages.

4.2. *Flame-element tracking*

According to classic flamelet theory, each point along the stoichiometric surface can be viewed as a discrete flame element with two possible states, *burning* or *extinguished*, with flame edges delimiting the burning and extinguished regions of the flame.

In the unperturbed flame all the flame elements are in the *burning* state. As the interaction proceeds, initially burning flame elements can be quenched when (E1) the local scalar dissipation rate grows above its critical extinction value, or (E2) a receding flame edge (extinction front) propagating along the stoichiometric surface passes through the flame element. The subsequent reignition of the flame elements may proceed through three different scenarios [28], namely when (I1) an advancing flame edge (ignition front) propagating along the stoichiometric surface passes through the flame element, healing or closing the hole, (I2) the scalar dissipation rate decreases below its critical ignition value, producing the spontaneous ignition of the flame, or (I3) an ignited flame element, or a hot pocket of reacted products, is brought into contact, through convection and diffusion, with the extinguished element for a sufficient amount of

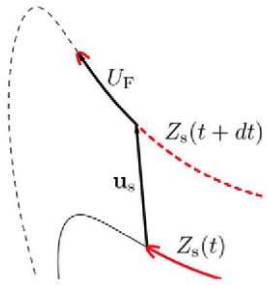

Fig. 4. The dynamics of the flame edges results from the superposition of the velocity, $\mathbf{u}_s$, of the stoichiometric surface with respect to the laboratory reference frame and the flame-edge propagation velocity along the stoichiometric surface, U_F.

time, thus facilitating the reignition of the mixed reactants. In strained diffusion flames, scenarios (I1) and (I3) are thought to be the main mechanisms responsible for flame creation after local flame extinction [28,55]. When the feeding streams are cold, as we assume here, the ignition delay time is too large compared to the characteristic residence time for spontaneous reignition to take place, and thus the autoignition mechanism (I2) can be safely excluded from the model.

As previously discussed, the local extinction of the flame leads to the apparition of flame edges separating the burning and extinguished regions. Each flame edge can be characterized by (i) its position $\mathbf{x}_F(\tau)$ on the stoichiometric surface and (ii) its orientation ϑ_F with respect to the local tangent vector $\mathbf{t}$, defined by a 90° clockwise rotation of the normal vector $\mathbf{n} = (\nabla Z/|\nabla Z|)_s$. Thus, we set $\vartheta_F = 1$ for ignition fronts propagating with positive velocity ($U_F > 0$) in the $\mathbf{t}$ direction, and $\vartheta_F = -1$ otherwise. According to this, the evolution of the flame-edge position, depicted in Fig. 4, is governed by the equation

$$\frac{d\mathbf{x}_F}{d\tau} = \mathbf{u}_s + \vartheta_F \tilde{u}_F \mathbf{t}, \tag{19}$$

where $\mathbf{u}_s$ is the velocity of the stoichiometric surface at $\mathbf{x}_F$, given by Eq. (15), and $\tilde{u}_F$ is the nondimensional front propagation velocity, namely

$$\tilde{u}_F = \frac{U_F}{A_0 r_0} = \frac{U_F}{S_L}\frac{S_L}{A_0 r_0}. \tag{20}$$

Here the normalized flame-edge velocity U_F/S_L can be evaluated from Eq. (17), while the ratio $S_L/(A_0 r_0)$ can be rewritten

$$\frac{S_L}{A_0 r_0} = \frac{D_T/\delta_L}{A_0 r_0} = \frac{D_T^{1/2}}{A_0^{1/2} r_0}\frac{(D_T/\chi_{s,0})^{1/2}}{\delta_L}\frac{\chi_{s,0}^{1/2}}{A_0^{1/2}}$$
$$= \frac{1}{\mathrm{Pe}_0^{1/2}}\mathrm{Da}_0^{1/2}\kappa^{1/2}(S)$$
$$= \left(\frac{\mathcal{R}}{\mathrm{Pe}_0}\right)^{1/2}\mathrm{Da}_e^{1/2}\kappa^{1/2}(S) \tag{21}$$

in terms of the nondimensional parameters $\mathcal{R}$, Pe_0, and Da_e, as well as the nondimensional scalar dissipation rate at the unperturbed flame,

$$\kappa(S) \equiv \frac{\chi_{s,0}}{A_0}$$
$$= \frac{1}{2\pi}\exp\left\{-2\left[\mathrm{erfc}^{-1}\left[2S/(S+1)\right]\right]^2\right\}, \tag{22}$$

a value that depends only on the overall stoichiometry. The parameter $\mathrm{Da}_0 = (D_T/\chi_{s,0})/\delta_L^2 = \mathcal{R}\mathrm{Da}_e$ appearing in (21) denotes the Damköhler number of the unperturbed flame.

As a final remark, two mechanisms that may lead to flame-edge annihilation will be discussed. First, when two ignition (or extinction) fronts propagating in opposite directions approach each other, they may eventually collide and disappear. Another mechanism of front annihilation occurs when the burning flame elements located in the vicinity of a receding flame front are suddenly extinguished by mechanism (E1). This happens if extinction takes place in a time sufficiently short compared to the time r_0/S_L employed by the front to propagate a distance of order r_0. However, in this case a new front with the same orientation will immediately appear at a certain distance from the previous front, as if it would have receded very rapidly. Even though in our analysis we account for the variable density effects in the triple-flame front velocity when the flame edges are far from each other, it cannot be very accurate for the description of the final stages of the annihilation of flame edges. However, we will see below that our model reproduces, at least in a qualitative way, all this phenomenology.

4.3. *Order-of-magnitude estimates*

The above discussion suggests that if we specify the composition of the feeding streams, and we are given the vortex size and strength, the dynamics of the flame edges appearing after local flame extinction is uniquely determined by the robustness parameter, $\mathcal{R} > 1$. Highly robust flames ($\mathcal{R} \gg 1$) require very strong vortices to be extinguished, while very weak flames ($\mathcal{R} - 1 \ll 1$) are completely extinguished as soon as they are perturbed. Thus, from a theoretical point of view the robust flame regime is by far the most interesting case of study, since it involves phenomena such as local flame extinction, flame-edge propagation, flame-hole/disc dynamics, flame reconnection, and pocket formation. Before proceeding with the numerical computations, we shall try to anticipate the parameter range where this regime applies, using order-of-magnitude estimates.

We consider the case of a highly robust flame perturbed by a vortex ring of radius r_0 that is assumed to be sufficiently strong to produce local flame extinction. We want to analyze the conditions for which the resulting flame edges can propagate into the extinguished region, thereby healing the flame, or, alternatively, recede toward the burning flame, leading to further flame extinction.

After local flame extinction, the flame develops an extinguished hole—or annulus—of characteristic size r_0. In order for the flame edges to be able to propagate into the extinguished region and act as ignition fronts that heal the hole and reconnect the flame, they must be able to propagate radially inward against the fluid located at $r \sim r_0$. Thus, the front velocity, U_F, which reaches values of order $U_F/S_L \lesssim f_\infty$ for $Da \gg 1$, must be at least of order $A_0 r_0$, i.e.,

$$\frac{A_0 r_0}{S_L} \sim \frac{U_F}{S_L} \lesssim f_\infty. \tag{23}$$

This inequality can also be viewed as a condition for the flame hole radius, or vortex size, r_0, which must be smaller or of the same order than the critical radius $r^* = f_\infty S_L/A_0$ that separates the shrinking and expanding hole regimes [53,54]. Substituting Eq. (21) in the above expression, we may write

$$\frac{1}{Da_e^{1/2}\kappa^{1/2}(S)}\left(\frac{Pe_0}{\mathcal{R}}\right)^{1/2} = \frac{A_0 r_0}{S_L} \lesssim f_\infty, \tag{24}$$

which, aside from constants of order unity, provides the scaling relation

$$\frac{Pe_0}{\mathcal{R}} \lesssim f_\infty^2. \tag{25}$$

It should be noted that the factor f_∞^2 appearing in (25) introduces a correction of order 10 in the admissible Peclet numbers, showing the importance of including heat release effects in the modeling of flame-edge dynamics.

Moreover, for sufficiently strong vortices, $\widetilde{\Gamma} \gg 1$, the unperturbed value of the scalar dissipation rate, $\chi_{s,0}$, and the maximum scalar dissipation rate experienced by the flame throughout the interaction, $\chi_{s,max} > \chi_{s,e}$, are related by

$$\mathcal{R} = \frac{\chi_{s,e}}{\chi_{s,0}} < \frac{\chi_{s,max}}{\chi_{s,0}} \sim \widetilde{\Gamma}, \tag{26}$$

where we have omitted a factor of order unity multiplying $\widetilde{\Gamma}$ (see VL for details). From Eq. (26) we derive the relation

$$Da_\Gamma \sim \frac{\mathcal{R}}{\widetilde{\Gamma}} \lesssim 1, \tag{27}$$

linking the values of $\widetilde{\Gamma}$ and $\mathcal{R}$.

On the other hand, we assume that under near-extinction conditions the structure of the thin reaction layer, with characteristic response time $1/(\chi_s\beta^2)$ small compared with $1/\chi_s$, is quasi-steady and quasi-planar throughout the interaction, β being the Zeldovich number, which is typically of order 10. The critical value of χ_s for extinction can then be taken to be equal to the extinction value $\chi_{s,e}$ of a planar steady diffusion flame, which can be obtained experimentally or using numerical calculations based on a detailed kinetic scheme. Nevertheless, unsteady effects play a key role in determining the evolution of the mixing layer structure, and therefore of χ_s, which in turn determines the conditions for local flame extinction.

Thus, if we define the mechanical time, $t_m = 1/\chi_{s,0}$, of the order of the inverse of the baseline strain rate, A_0, the characteristic response time of the reaction layer, $t_r = 1/(\chi_{s,e}\beta^2)$, and the characteristic vortex turnover time, $t_T = 2r_0^2/\Gamma$, we shall assume the ordering $t_r \lesssim t_T \lesssim t_m$, meaning that the vortex introduces unsteady effects into the outer diffusive–convective layer, while the inner reactive–diffusive layer behaves in a quasi-steady manner, since the characteristic chemical time is still much shorter than the characteristic time induced by the vortex. In terms of $\widetilde{\Gamma}$, $\mathcal{R}$, and β, this ordering can alternatively be written as

$$\frac{1}{\mathcal{R}\beta^2} \lesssim \frac{1}{\widetilde{\Gamma}} \lesssim 1 \quad \Rightarrow \quad Da_\Gamma \sim \frac{\mathcal{R}}{\widetilde{\Gamma}} \gtrsim \frac{1}{\beta^2}. \tag{28}$$

According to this, for nontrivial quasi-steady-extinction/reignition dynamics to occur, all three conditions, (25), (27), and (28), must be simultaneously satisfied.

Many of the theoretical considerations discussed above were derived based on assumptions that may not be valid for $\widetilde{\Gamma}$ large enough for the laminar vortex to become unstable or turbulent. This point was briefly discussed in our previous work (VL) and deserves an additional comment here.

Due to the instability of vortex rings to azimuthal bending waves, the results presented in this paper are limited to values of the Reynolds number $A_I\delta_v^2/\nu$, based on the vortex core size, δ_v, and the self-induced strain, A_I, experienced by the core, below a certain critical value $(A_I\delta_v^2/\nu)_{crit} \simeq 60$ (see Widnall and Tsai [56] and Saffman [57] for details). Using the expression for the self-induced strain given by Saffman [57, Eq. (4.2)],

$$A_I = \frac{3\Gamma}{16\pi r_0^2}\left[\log\left(\frac{8r_0}{\delta_v}\right) - \frac{17}{12}\right], \tag{29}$$

and the size of the vortex core $\delta_v^2 = 8\nu/A_0$ given by Eq. (6), the above stability criterion becomes

$$\frac{A_I\delta_v^2}{\nu} = 6\left(\frac{\Gamma}{2r_0^2A_0}\right)\frac{1}{2\pi}\left[\log\left(\frac{8r_0}{\delta_v}\right) - \frac{17}{12}\right]$$

$$\lesssim \left(\frac{A_1\delta_v^2}{\nu}\right)_{\text{crit}} \simeq 60 \tag{30}$$

or, alternatively,

$$\widetilde{\Gamma} \lesssim \frac{10}{\alpha_0 - C'}, \tag{31}$$

where α_0 is given by Eq. (4) and $C' = (17/12 - 0.558)/2\pi = 0.137$ for a Gaussian vorticity core. It is easy to check that all the results presented below verify condition (31). For instance, in the most restrictive case presented in this paper, corresponding to $\mathrm{Pe}_0 = 80$, the maximum value of $\widetilde{\Gamma}$ typical for a laminar vortex, as given by condition (31), is about $\widetilde{\Gamma} \approx 32$, which guarantees the existence of the distinguished regime of laminar vortices with $\widetilde{\Gamma} \gg 1$.

It is important to note that the stability criterion (31) corresponds to freely propagating vortex rings, and therefore it does not account for the effect of the azimuthal stretching experienced by the vorticity core due to the growth of the vortex ring radius. This stretching is believed to act as a stabilizing effect, so that the range of applicability of the theoretical model predicted in (31) should be viewed as conservative.

It is important to note that the order of magnitude estimates presented in this section, leading to conditions (25), (27), and (28), could be used to extend existing diagrams of diffusion-flame/vortex interaction regimes [21] in the limit of strong vortices considered here.

5. Numerical method

The spatial and temporal evolution of the mixture fraction field is obtained from numerical integration of Eq. (9) using a 16th-degree finite-difference method for the spatial derivatives [58] and a classical fourth-order Runge–Kutta method for the temporal evolution.

The computational domain, extending from $\xi_{\min} = 0$ (symmetry axis) to $\xi_{\max} = 5$, and from $\eta_{\min} = -1$ to $\eta_{\max} \approx 10$, is discretized using a Cartesian rectangular grid whose nodes are distributed nonuniformly according to the method described in [58]. The symmetry condition $\nabla Z \cdot \mathbf{n}_{\text{bc}} = 0$ is imposed at $\xi = 0$, where $\mathbf{n}_{\text{bc}}$ is the normal vector pointing outwards of the computational domain. At the remaining boundaries a purely convective boundary condition is employed, for which the condition $Z = Z_0(\eta)$ holds whenever $\mathbf{v} \cdot \mathbf{n}_{\text{bc}} < 0$, while no condition needs to be specified when the flow exits the domain.

The number of grid nodes and the size of the time step, typically $N_\xi \approx 200$, $N_\eta \approx 400$, and $\Delta\tau \approx 10^{-4}$, result from a sequence of simulations with increasing spatial and temporal accuracy, until a three-digit match is achieved between consecutive simulations. To avoid the singularities introduced by the potential flow assumption, a regularized form of the velocity field $\mathbf{v}$ has been used (see Appendix A for details).

After computing the evolution of the mixture fraction field, the stoichiometric isosurface is extracted and discretized at each time step by means of a set of uniformly spaced discrete flame-elements, with uniform nondimensional spacing equal to 10^{-3}. In the simulations presented below, the number of flame elements grows from 5000 in the initial unperturbed flame up to 15,000 in the most strongly distorted flames at later stages of the interaction. In addition, we use a third-order interpolant to evaluate the scalar dissipation rate χ_s and the flame-sheet velocity $\mathbf{u}_s$ corresponding to each flame element at every time step.

Flame-element tracking is carried out by integrating the evolution equation for a point on the stoichiometric surface,

$$\frac{d\mathbf{x}_s}{d\tau} = \mathbf{u}_s, \tag{32}$$

using a classical second-order implicit Adams–Moulton method. To establish a one-to-one correspondence between flame elements at different time steps, the implicit numerical scheme is directly applied to pairs of flame elements $\mathbf{x}_{s,i}^n$ and $\mathbf{x}_{s,j}^{n+1}$ at successive time steps, n and $n+1$, and used as an error estimator to calculate

$$\mathcal{E}\left(\mathbf{x}_{s,i}^n, \mathbf{x}_{s,j}^{n+1}\right) = \left\| \left(\mathbf{x}_{s,i}^n + \frac{\Delta\tau}{2}\mathbf{u}_{s,i}^n\right) - \left(\mathbf{x}_{s,j}^{n+1} - \frac{\Delta\tau}{2}\mathbf{u}_{s,j}^{n+1}\right) \right\|, \tag{33}$$

binding those flame elements that minimize this error.

After calculating the time evolution of the flame elements, we can study the phenomena of local flame extinction and flame-edge dynamics. Initially, all flame elements are in a burning state. However, as the interaction evolves, the state of certain flame elements may change to extinguished if the normalized local scalar dissipation rate, $\chi_s/\chi_{s,0}$, exceeds its critical extinction value, $\chi_{s,e}/\chi_{s,0} = \mathcal{R}$. The evolution of the resulting flame-edges along the stoichiometric surface is given by

$$\frac{d\mathbf{x}_F}{d\tau} = \vartheta_F \tilde{u}_F \mathbf{t}, \tag{34}$$

which corresponds to the second contribution to the front movement in (19). The above equation can be integrated numerically using an explicit Euler method to obtain the flame-edge position, thus allowing us

to update the burning/nonburning state of the corresponding flame elements following the scenarios discussed in Section 4.

6. Discussion of results

To show the capabilities of the mathematical model described in the previous sections, the numerical results where compared with selected experimental visualizations available in the literature. In all the cases presented below, the experimental conditions lead to nondimensional parameters Pe_0 and $\widetilde{\Gamma}$, that render our model applicable.

6.1. *Infinitely robust flames*

Fig. 5 displays a sequence of snapshots showing the evolution of the reacting mixing layer at regular time intervals. The flame sheet, shown as a thick solid line, is plotted on top of the corresponding mixture fraction isocontours, with dark gray standing for $Z = 0$ and light gray for $Z = 1$. The values of the nondimensional parameters, $\mathrm{Pe}_0 = 80$, $\widetilde{\Gamma} = 20$, $S = 0.7$, and $\mathcal{R} \to \infty$, have been selected so as to match the experimental conditions of Case 2 in Ref. [15]. It is important to note that in all the experimental cases considered in this paper the fuel stream is strongly diluted with nitrogen, so that the density ratio ρ_F/ρ_{O_2} is close to one, as assumed in our model. As a consequence, we observe good qualitative agreement between the evolution of the flame sheet predicted by the mathematical model and the experimental visualizations given in Fig. 11 of [15]. This demonstrates the validity of the presumed velocity field and the ability of Eq. (9) to describe the mixture fraction field.

The first frame in Fig. 5 ($\tau = -0.25$) shows the mixing layer in its unperturbed state. Due to the large self-induced velocity of the vortex, $\widetilde{\Gamma} \gg 1$, in the second frame ($\tau = 0.05$) the vortex ring crosses, without significant change in its structure, the original position of the mixing layer. This is simultaneously displaced and wrapped around the bubble of fluid moving with the vortex ($\tau = 0.35$), leaving behind a flame stem that shrinks with time ($\tau = 0.75$), which eventually disappears by mutual annihilation of the flame elements near the symmetry axis ($\tau = 1.05$). Clearly, in this case the strength of the vortex is not sufficient to trigger the local extinction of the flame ($\widetilde{\Gamma} \ll \mathcal{R}$), but is large enough to generate an ignited pocket of reactant that travels with the vortex, which will burn completely in times on the order of the diffusion time r_0^2/D_T, or, in dimensionless form, of order $\tau \sim A_0 r_0^2/D_T \sim \mathrm{Pe}_0$.

It is worth noting that this interpretation of the results is somewhat different to that given in [15], where the vortex ring crosses the diffusion flame and enters the upper nozzle. What they describe as an outer reacting ring left behind by the vortex corresponds in our interpretation to the vortex ring with the rolled-up flame, which in our case neither crosses the diffusion flame nor enters the upper nozzle.

6.2. *Annular extinction events*

Figs. 6a and 6b show the development of two annular extinction events induced by a strong vortex in a robust flame. The values of the nondimensional parameters, $\mathrm{Pe}_0 = 60$, $\widetilde{\Gamma} = 30$, and $S = 1.5$, were selected to match the experimental conditions of Flame E in [31] or, equivalently, Flame A in [34]. Two values of $\mathcal{R}$ where considered, namely $\mathcal{R} = 25$ (upper plot) and $\mathcal{R} = 14.5$ (lower plot). In all the figures presented below, the point of maximum scalar dissipation rate $\chi_{s,\max}$ (where local flame extinction may eventually occur) is marked by a circle, and the

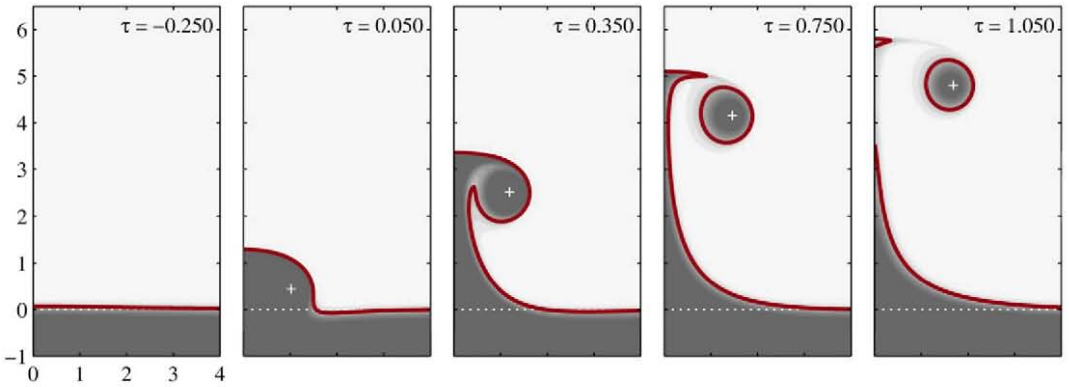

Fig. 5. Flame-sheet evolution in a flame/vortex interaction with $\mathrm{Pe}_0 = 80$, $\widetilde{\Gamma} = 20$, $S = 0.7$, and $\mathcal{R} \to \infty$. Parameter values derived from the experimental conditions of Case 2 in [15]. Thick solid lines: flame sheet.

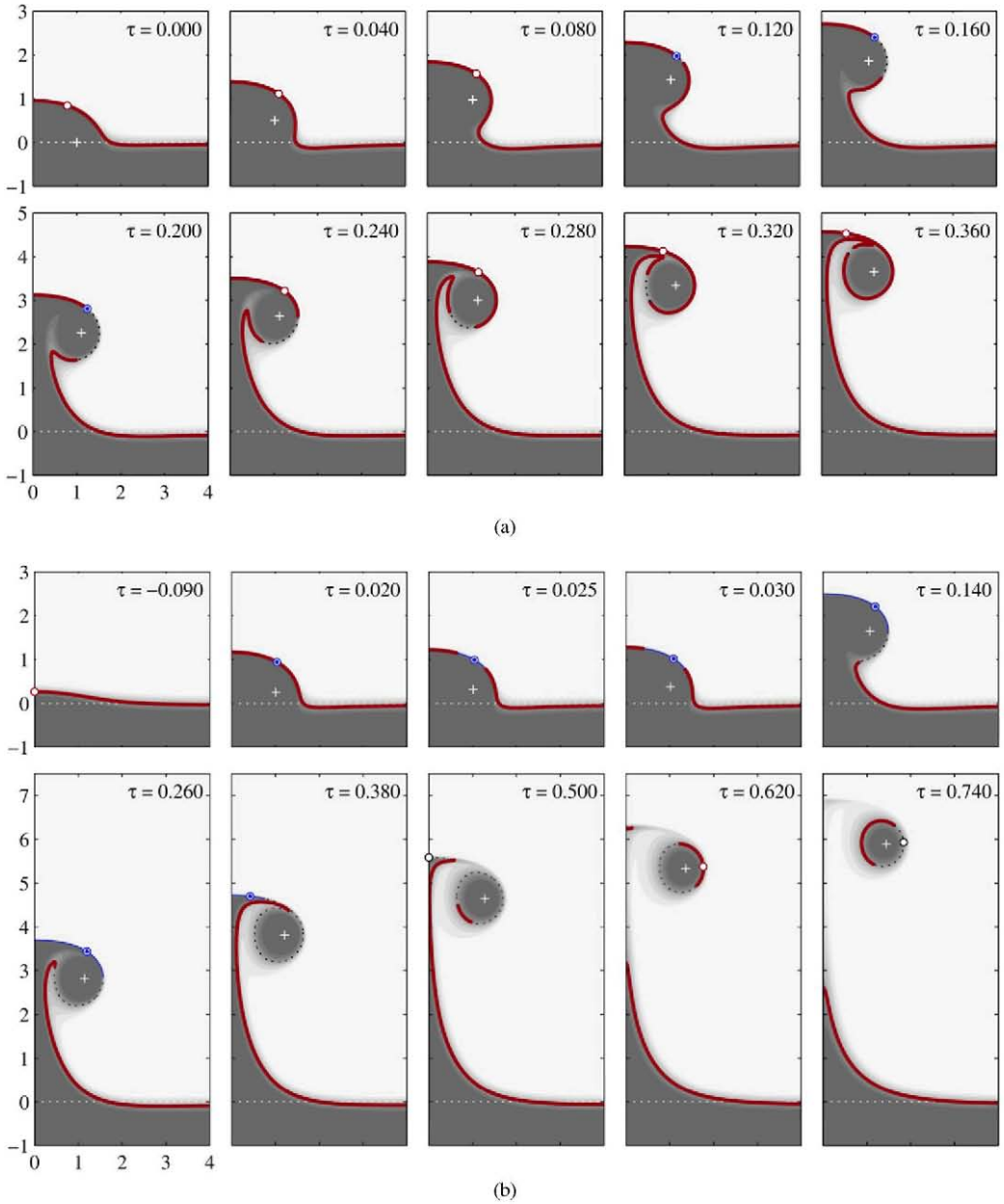

Fig. 6. Flame-sheet evolution in a flame/vortex interaction with $\mathrm{Pe}_0 = 60$, $\widetilde{\Gamma} = 30$, $S = 1.5$ for (a) $\mathcal{R} = 25$ and (b) $\mathcal{R} = 14.5$. Parameter values chosen to match the experimental conditions of Flame E in [31] or Flame A in [34]. Thick solid lines: flame sheet; thin solid lines: extinguished flame elements with $\chi_s > \chi_{s,e}$; thin dotted lines: extinguished flame elements with $\chi_s < \chi_{s,e}$; filled circle (hollow circle): location of maximum scalar dissipation rate, $\chi_{s,\max} > \chi_{s,e}$ ($\chi_{s,\max} < \chi_{s,e}$). The mixture fraction field is shown in grayscale for illustrative purposes.

region where $\chi_s > \chi_{s,e}$ (where the flame must necessarily be extinguished) is shown in thin solid lines.

The sequences of Figs. 6a and 6b both exhibit annular extinction patterns that leave an isolated burning disk ahead of the vortex. The subsequent evolution of the burning disk depends on the overall Damköhler number, $\mathrm{Da}_I \sim \mathcal{R}/\widetilde{\Gamma}$. In Fig. 6a the disk initially shrinks in size ($\tau = 0.16$), but as soon as the local scalar dissipation rate decreases below its extinction value ($\tau = 0.24$), the disk recovers and starts to grow, assisted by the flow induced by the vortex, until the flame eventually burns back around the vortex ($\tau = 0.28$–0.36). In Fig. 6b, the extinguished region soon reaches the axis due to the high strain rates imposed

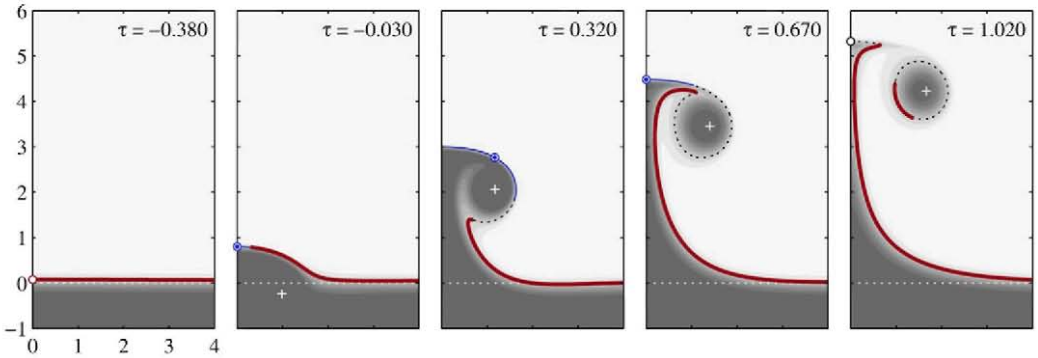

Fig. 7. Flame sheet evolution in a flame/vortex interaction with $\mathrm{Pe}_0 = 40$, $\widetilde{\Gamma} = 20$, $S = 0.5$, and $\mathcal{R} = 5.5$. Parameter values derived from the experimental conditions of Case 1 in [15]. See caption of Fig. 6 for details.

in front of the vortex, where all flame elements experience scalar dissipation rates above its extinction value. The remaining flame then travels up the stem pulled by the vortex, getting anchored in the fold that forms between the stem and the vortex. Immediately before pinch-off, a small flame element reaches the vortex core, generating two ignition fronts that eventually heal the flame.

A direct comparison of Figs. 6a and 6b with Figs. 11 and 10, respectively, of Ref. [31] shows that the present results are in good agreement with the experimental observations reported there (see also Ref. [34] for further experimental results to compare with). However, later stages of the interaction do not match well due to the presence of the jet that follows the (starting) vortex ring generated in the experimental setup. Nevertheless, the correct prediction of the annular extinction phenomenon shows that local flame extinction can be solely triggered by an excess in the local scalar dissipation rate, whose maximum value is attained in this case off the symmetry axis. Remember that the analysis presented here is based on the assumption of unity Lewis numbers, and therefore does not include preferential diffusion effects. This demonstrates that annular extinction events do not necessarily result from the combined effects of preferential diffusion and curvature, as previously stated in Ref. [14].

6.3. Axial extinction followed by reignition via edge flames

Fig. 7 shows an axial extinction event that occurs for $\mathrm{Pe}_0 = 40$, $\widetilde{\Gamma} = 20$, $S = 0.5$, and $\mathcal{R} = 5.5$, a set of parameter values selected to match the experimental conditions of Case 1 in [15]. As can be seen, while the strength of the vortex is slightly reduced compared to that of the previous section, the robustness of the flame is much less, leading to an axial extinction ($\tau = -0.03$) even before the vortex crosses the plane $z = 0$. These results are in good agreement with the experimental images depicted in Fig. 10 of Ref. [15].

It should be noted that the long-term evolution of the flames shown in Figs. 6b and 7 is very similar regardless of the value of $\mathcal{R}$. As previously discussed, this is due to the fact that for large $\widetilde{\Gamma}$ the dynamics of the flame edges is mostly governed by the strong convective velocities imposed by the vortex, being much less affected by the robustness of the flame. However, if for fixed values of Pe_0 and $\widetilde{\Gamma}$ the robustness parameter is further decreased, different long-term evolutions may be observed, ranging from the formation of unburned pockets to the complete extinction of the flame, reached as $\mathcal{R}$ approaches its limiting value $\mathcal{R} = 1$.

As already suggested in VL, axial extinction is much more likely to occur than annular extinction. While axial extinction always occurs for sufficiently small values of $\mathrm{Da}_\Gamma \sim \mathcal{R}/\widetilde{\Gamma}$, annular extinction can only be observed within a narrow band of values of this parameter, slightly below $\mathcal{R}/\widetilde{\Gamma} = 1$, depending on α_0. In addition, due to the rapid recession of the flame after an annular extinction event, high temporal resolution imaging may be required to obtain sequential images of these phenomena, as clearly illustrated by the elapsed times reported in the snapshots shown in Fig. 6 and in the experimental results of Refs. [31,34].

6.4. Case of weak flames

The rich phenomenology observed in the interaction of strong vortices with flames discussed in the previous sections is mainly characteristic of H_2–air flames. Due to the high reaction rates and molecular diffusivity, H_2–air mixtures are about 30 times stronger than CH_4–air measured in terms of extinction strain rates [59]. This has enabled to investigate the response of highly robust flames to strong

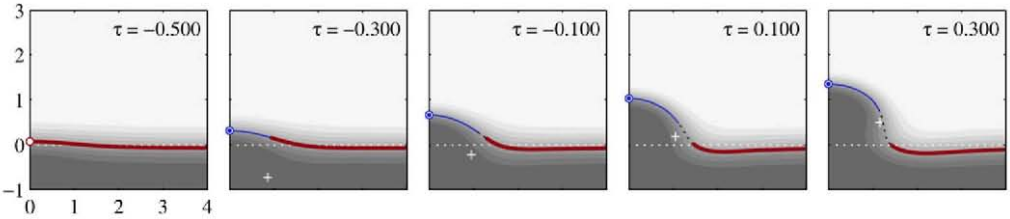

Fig. 8. Flame-sheet evolution in a flame/vortex interaction with $\mathrm{Pe}_0 = 10$, $\widetilde{\Gamma} = 7$, $S = 1.35$, and $\mathcal{R} = 1.5$. Parameter values derived from the experimental conditions presented in [16]. See caption of Fig. 6 for details.

perturbations in the experimental literature (e.g., [15,31,34]).

For fuels other than H_2, the characteristic values of the scalar dissipation rate (or, alternatively, the strain rate) at extinction are substantially lower than those for H_2. In the literature, therefore, one typically encounters weak flames ($\mathcal{R} - 1 \sim 1$) interacting with weak vortices (Santoro et al. [16]).

In order to check the ability of our model to simulate weak-flame/weak-vortex interactions, we present in Fig. 8 the development of an axial extinction event ($\tau = -0.3$) induced by a vortex ring in a diffusion flame. The parameter values correspond approximately to the experimental methanol-air flame/vortex interactions studied by Santoro et al. [16]. (Precise values for all the nondimensional parameters cannot be obtained from the incomplete experimental conditions reported in [16].) Due to the relatively small Reynolds number of the vortex, $\widetilde{\Gamma}\mathrm{Pe}_0 = 70$, the assumed velocity field is expected to fail relatively soon, so that larger discrepancies with the experimental results are anticipated in this case.

Nevertheless, the qualitative agreement with the experimental results shown in Fig. 2 of Ref. [16] is still quite satisfactory during the first interaction stages. Unlike the strong vortices discussed previously, the weak vortex is not able to wrap the flame. Instead, it penetrates the thick mixing layer ($\tau = 0.1$), and eventually crosses the flame ($\tau > 0.3$). Note that for small values of the Peclet number ($\mathrm{Pe}_0 = 10$), the thickness of the unperturbed mixing layer is of the order of the characteristic vortex ring radius. In this case, the vortex ring is expected to dissipate rapidly as it comes into contact with the hot gases of the mixing layer, a process that cannot be accurately described with our constant-property model for the velocity field (see VL for details). This leads to growing discrepancies between the theoretical and experimental results, specially for large times.

Thus, while the experimental flame was observed to restore itself [16] after local flame extinction, presumably due to the complete dissipation of the vortex, the theoretical model predicts the complete extinction of the flame after being swept out by the vortex ring, which grows indefinitely in radius and does not dissipate. These discrepancies can not be seen in Fig. 8, which only illustrates the first stages of the interaction.

6.5. *Time evolution of integral magnitudes*

Two global measurements of the diffusion-flame/vortex interaction are the time evolution of the overall flame surface area, $\mathcal{S}$, and the fuel consumption rate, $\dot{m}_\mathrm{F}$. These parameters are good indicators of the flame response, including local extinction and reignition phenomena. For comparison purposes, the instantaneous values of $\mathcal{S}(\tau)$ and $\dot{m}_\mathrm{F}(\tau)$ can be normalized by subtracting the values at the unperturbed flame, $\mathcal{S}_0$ and $\dot{m}_{\mathrm{F}0}(\tau)$, and dividing the result by the reference surface area, πr_0^2, and fuel consumption rate, $\pi r_0^2 \dot{m}''_{\mathrm{F}0}$, respectively, where $\dot{m}''_{\mathrm{F}0} = \rho Y_{\mathrm{F}0}(D_\mathrm{T} A_0)^{1/2}(1 + S^{-1})\kappa^{1/2}(S)$ denotes the fuel consumption rate per unit flame surface at the unperturbed flame.

Fig. 9 shows the time evolution of the normalized flame surface area, $\widetilde{\mathcal{S}} = [\mathcal{S}(\tau) - \mathcal{S}_0]/(\pi r_0^2)$, and fuel consumption rate, $\widetilde{\dot{m}}_\mathrm{F} = [\dot{m}_\mathrm{F}(\tau) - \dot{m}_{\mathrm{F}0}]/(\pi r_0^2 \dot{m}''_{\mathrm{F}0})$, corresponding to the cases illustrated in Fig. 6. Also shown is the evolution of $\widetilde{\mathcal{S}}$ and $\widetilde{\dot{m}}_\mathrm{F}$ in the limiting case, $\mathcal{R} \to \infty$, when the flame is not extinguished, included here for reference purposes.

The time evolution of integral flame magnitudes such as $\widetilde{\mathcal{S}}$ or $\widetilde{\dot{m}}_\mathrm{F}$ is strongly affected by the vortex. During the first stages of the interaction, before local flame extinction occurs, both magnitudes start to grow as a consequence of the flame straining and distortion introduced by the vortex. Local flame extinction is characterized by a sharp drop of flame surface area and fuel consumption rate, which is less prominent in the more robust flame that in addition is extinguished later. In the absence of extinction, $\widetilde{\mathcal{S}}$ and $\widetilde{\dot{m}}_\mathrm{F}$ increase smoothly (dashed lines), reaching values of order 14 and 28, respectively. As the locally extinguished flame is displaced and wrapped around the vortex ring, both $\widetilde{\mathcal{S}}$ and $\widetilde{\dot{m}}_\mathrm{F}$ start to increase again, until another sharp transition occurs, coinciding with the collapse of the stem and the vortex pinch-off. The wriggles that appear in

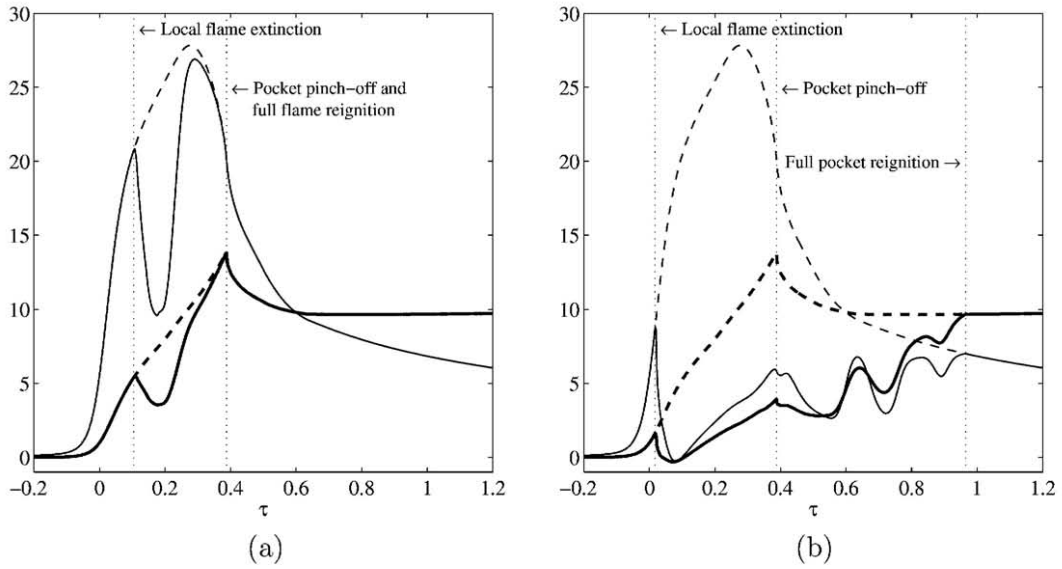

Fig. 9. Time evolution of the normalized flame surface area, $\widetilde{\mathcal{S}}$ (thick solid lines), and fuel consumption rate, $\widetilde{m}_{\mathrm{F}}$ (thin solid lines), in a flame/vortex interaction with $\mathrm{Pe}_0 = 60$, $\widetilde{\Gamma} = 30$, $S = 1.5$ for (a) $\mathcal{R} = 25$ and (b) $\mathcal{R} = 14.5$ (see Fig. 6). Also shown is the evolution of $\widetilde{\mathcal{S}}$ (thick dashed lines) and $\widetilde{m}_{\mathrm{F}}$ (thin dashed lines) in the limit $\mathcal{R} \to \infty$, when the vortex is not able to extinguish the flame. Local extinction/reignition phenomena occur where indicated.

Fig. 6b in the range $0.4 < \tau < 1$ are due to the spinning of the partially ignited flame around the vortex.

Once the flame is completely reignited, the smooth evolution of the flame area is determined by a balance between the growth of the vortex core radius and the diffusive decrease of the mixture fraction at the core. The former tends to increase the flame surface area, while the latter tends to reduce it. Which of the two trends dominates depends mainly on the overall stoichiometry S. In the particular case illustrated in Fig. 9 both mechanisms are seen to balance almost perfectly for $\tau \sim 1$, although diffusion will always take over for sufficiently long times, when the flame surface area will return to its initial value.

7. Conclusions

A mathematical model is presented to describe local flame extinction and reignition in a gaseous counterflow diffusion flame perturbed by a laminar vortex ring, with emphasis on the dynamics of the flame edges that form after local flame extinction between the burning and extinguished regions of the flame.

The analysis is based on a simplified description of the velocity field derived from potential flow theory. However, in order to avoid the potential divergence of the azimuthal velocity at the vortex core, the flow field is regularized near the core using a Gaussian vorticity profile obtained from previous asymptotic analysis.

In the Burke–Schumann limit of infinitely fast chemistry the problem can be reduced to one of mixing, involving the classical mixture fraction Z, whose solution provides the flame-sheet location as well as the local combustion rate, given by the local value of the scalar dissipation rate χ_{S}. Aside from the constant density approximation, the main assumption of the model is that the flame edges generated after local flame extinction propagate with a well-defined velocity that is a function of the local Damköhler number, $\mathrm{Da} = 1/(\chi_{\mathrm{S}} t_{\mathrm{L}})$. The flame-edge velocity is then modeled using a synthetic analytic expression motivated by recent numerical results on triple- and edge-flame propagation in mixing layers with heat release effects fully taken into account [51].

The most interesting case of study corresponds to the so-called robust flame regime, $\mathcal{R} \gg 1$. In this regime the dynamics of the flame edges is mainly driven by the strong convective velocities induced by the vortex ring, and the model reproduces phenomena such as local flame extinction, flame holes, edge flames, and—in some cases—flame reconnection and pocket formation. On the other hand, in the weak flame regime, $\mathcal{R} - 1 \ll 1$, the flame is completely extinguished as soon as it is perturbed by the vortex, and thus does not show any relevant flame-edge dynamics.

Despite its apparent simplicity, the model reveals the main nondimensional parameters that characterize the evolution of the flame sheet and the local flame extinction/reignition phenomena, capturing and clarifying most parametric dependencies experimentally

observed in nonpremixed flame/vortex interactions. The agreement with previously published experimental results is good, demonstrating the potential of the model to describe extinction and reignition phenomena in unsteady nonpremixed systems.

The analysis presented here provides a simple theoretical framework appropriate to analyze relevant phenomena such as axial/annular extinction, different reignition scenarios, flame-edge dynamics, pocket formation, and noise generation. However, further work is needed to clarify the effects of preferential diffusion and thermal expansion on the obtained results. A similar modeling approach could also be useful to investigate spray/particle combustion or to validate reduced kinetics models in realistic unsteady flow fields.

Acknowledgments

This collaborative research was supported by the Spanish MEC under Projects #ENE2005-08580-C02-01 and ENE2005-09190-C04-01 and by the Comunidad de Madrid under Project #S-505/ENE/0229. The authors are indebted to Dr. E. Fernández-Tarrazo at the Spanish *Instituto Nacional de Técnica Aeroespacial* (INTA) for helpful discussions. Part of the work of the senior author was carried out at Yale University, in cooperation with Professor A. Gomez and coworkers, during his stays as Adjunct Professor. M.V. would also like to thank Professor A. Gomez and Dr. Giuliano Amantini for their hospitality during a short stay at Yale University.

Appendix A. Regularization of the velocity near the vortex core

The axisymmetric velocity field described by Eq. (1) results from the superposition of the unperturbed strain and the inviscid flow induced by the vortex ring outside the vorticity core. The assumption of potential flow implies infinite velocities at the core, a singular behavior that has to be smoothed out before Eq. (9) is integrated. This can be easily done by matching the outer inviscid velocity field with an inner viscous solution at distances of the order of the nondimensional size, $\delta_v = (8\mathrm{Pr}/\mathrm{Pe}_0)^{1/2}$, of the vortex core. As inner viscous solution we use the Gaussian vorticity core employed, as in VL, for the determination of the nondimensional self-induced velocity α_0, which yields the regularized expressions for the velocity field

$$\tilde{u} = \frac{\xi}{2} + \frac{\widetilde{\Gamma}}{\pi\xi_c}\left(\frac{\xi_c}{2\xi}\right)^{3/2}\left(\frac{\eta-\eta_c}{\xi_c}\right)I_1(\mu) \times \left[1 - e^{-(\varrho/\delta_v)^2}\right], \tag{A.1a}$$

$$\tilde{v} = -\eta - \frac{\widetilde{\Gamma}}{\pi\xi_c}\left(\frac{\xi_c}{2\xi}\right)^{3/2}\left[\frac{\xi}{\xi_c}I_1(\mu) - I_0(\mu)\right] \times \left[1 - e^{-(\varrho/\delta_v)^2}\right], \tag{A.1b}$$

where $\varrho = [(\xi-\xi_c)^2 + (\eta-\eta_c)^2]^{1/2}$ denotes the nondimensional distance to the center of the vortex core. In the vicinity of the vortex core the above expressions must by substituted by the corresponding asymptotic expansions for $\varrho/\delta_v \ll 1$, namely

$$\tilde{u} = \frac{\xi}{2} + \frac{\widetilde{\Gamma}}{\pi\xi_c}\left(\frac{\eta-\eta_c}{\xi_c}\right)\left(\frac{\xi_c}{\delta_v}\right)^2 + O\left[\left(\frac{\varrho}{\delta_v}\right)^2\right], \tag{A.2a}$$

$$\tilde{v} = -\eta - \frac{\widetilde{\Gamma}}{\pi\xi_c}\left(\frac{\xi-\xi_c}{\xi_c}\right)\left(\frac{\xi_c}{\delta_v}\right)^2 + O\left[\left(\frac{\varrho}{\delta_v}\right)^2\right]. \tag{A.2b}$$

As a consequence of the simultaneous vanishing of ξ, I_0, and I_1 at the symmetry axis, the velocity field cannot be directly evaluated using (A.1) in this region. Again, the indetermination can be resolved by expanding asymptotically the velocity field for small values of ξ/ξ_c, namely

$$\tilde{u} = \frac{\xi}{2} + \frac{\widetilde{\Gamma}}{\pi\xi_c}\left[\frac{3}{2}\frac{\pi\hat{\eta}}{(1+\hat{\eta}^2)^{5/2}}\left(\frac{\xi}{\xi_c}\right)\right] + O\left[\left(\frac{\xi}{\xi_c}\right)^3\right], \tag{A.3a}$$

$$\tilde{v} = -\eta + \frac{\widetilde{\Gamma}}{\pi\xi_c}\left[\frac{\pi}{(1+\hat{\eta}^2)^{3/2}} - \frac{3}{4}\frac{\pi(4\hat{\eta}^2-1)}{(1+\hat{\eta}^2)^{7/2}}\left(\frac{\xi}{\xi_c}\right)^2\right] + O\left[\left(\frac{\xi}{\xi_c}\right)^4\right], \tag{A.3b}$$

where $\hat{\eta} = (\eta-\eta_c)/\xi_c$.

By applying Eqs. (A.1)–(A.3) in their respective domains of validity, a well-suited set of expressions for the velocity field is obtained.

References

[1] F.E. Marble, J.E. Broadwell, Project SQUID Technical Report TRW-9-PU, Project SQUID Headquarters, Chaffee Hall, Purdue University, 1977.

[2] P.H. Renard, D. Thévenin, J.C. Rolon, S. Candel, Prog. Energy Combust. Sci. 26 (2000) 225–282.

[3] F.E. Marble, in: C. Casci, C. Bruno (Eds.), Recent Advances in Aerospace Sciences, Plenum, New York, 1985, pp. 395–413.

[4] A.R. Karagozian, F.E. Marble, Combust. Sci. Technol. 45 (1986) 65–84.
[5] A.R. Karagozian, B.V.S. Manda, Combust. Sci. Technol. 49 (1986) 185–200.
[6] N. Peters, F.A. Williams, Proc. Combust. Inst. 22 (1988) 495–503.
[7] A.M. Laverdant, S. Candel, Combust. Sci. Technol. 60 (1988) 79–96.
[8] A.M. Laverdant, S. Candel, J. Propuls. Power 5 (1989) 134–143.
[9] D. Thévenin, S. Candel, Phys. Fluids 7 (1995) 434–445.
[10] F. Takahashi, V.R. Katta, J. Propuls. Power 11 (1995) 170–177.
[11] J.C. Rolon, F. Aguerre, S. Candel, Combust. Flame 100 (1995) 422–429.
[12] D. Thévenin, J.C. Rolon, P.H. Renard, D.W. Kendrick, D. Veynante, S. Candel, Proc. Combust. Inst. 26 (1996) 1079–1086.
[13] D. Thévenin, P.H. Renard, J.C. Rolon, S. Candel, Proc. Combust. Inst. 27. (1998) 719–726.
[14] V.R. Katta, C.D. Carter, G.J. Fiechtner, W.M. Roquemore, J.R. Gord, J.C. Rolon, Proc. Combust. Inst. 27 (1998) 587–594.
[15] P.H. Renard, J.C. Rolon, D. Thévenin, S. Candel, Combust. Flame 117 (1999) 189–205.
[16] V.S. Santoro, D.C. Kyritsis, A. Liñán, A. Gomez, Proc. Combust. Inst. 28 (2000) 2109–2116.
[17] V.S. Santoro, A. Liñán, A. Gomez, Proc. Combust. Inst. 28 (2000) 2039–2046.
[18] T. Poinsot, D. Veynante, S. Candel, Proc. Combust. Inst. 23 (1990) 613–619.
[19] T. Poinsot, D. Veynante, S. Candel, J. Fluid Mech. 228 (1991) 561–605.
[20] W.L. Roberts, J.F. Driscoll, M.C. Drake, L.P. Goss, Combust. Flame 94 (1993) 58–62.
[21] D. Thévenin, P.H. Renard, G.J. Fiechtner, J.R. Gord, J.C. Rolon, Proc. Combust. Inst. 28 (2000) 2101–2108.
[22] N. Peters, Turbulent Combustion, Cambridge Univ. Press, Cambridge, UK, 2000.
[23] A. Liñán, in: C.F. Brauner, C. Schmidt-Lainé (Eds.), Mathematical Modeling in Combustion and Related Topics, in: NATO ASI Series E, vol. 140, Martinus Nijhoff, The Netherlands, 1988, pp. 151–154.
[24] J.W. Dold, Combust. Flame 76 (1989) 71–88.
[25] G.R. Ruetsch, L. Vervisch, A. Liñán, Phys. Fluids 7 (1995) 1447–1454.
[26] L. Vervisch, T.J. Poinsot, Annu. Rev. Fluid Mech. 30 (1998) 655–692.
[27] C. Pantano, J. Fluid Mech. 514 (2004) 231–270.
[28] P. Sripakagorn, S. Mitarai, G. Kosály, H. Pitsch, J. Fluid Mech. 518 (2004) 231–259.
[29] H. Phillips, Proc. Combust. Inst. 10 (1965) 1277–1283.
[30] P.N. Kioni, B. Rogg, K.N.C. Bray, A. Liñán, Combust. Flame 95 (1993) 276–290.
[31] G.J. Fiechtner, C.D. Carter, K.D. Grinstead Jr., J.R. Gord, J.M. Donbar, J.C. Rolon, in: Fall Meeting of the Western States Section/The Combustion Institute, The Combustion Institute, 1998, Paper Number 98F–10.
[32] M.L. Shay, P.D. Ronney, Combust. Flame 112 (1998) 171–180.
[33] V.S. Santoro, A. Gomez, Proc. Combust. Inst. 29 (2002) 585–592.
[34] T.R. Meyer, G.J. Fiechtner, S.P. Gogineni, J.C. Rolon, C.D. Carter, J.R. Gord, Exp. Fluids 36 (2004) 259–267.
[35] G. Amantini, J.H. Frank, A. Gomez, Proc. Combust. Inst. 30 (2005) 1679–1685.
[36] N. Peters, Combust. Sci. Technol. 30 (1983) 1–17.
[37] J. Buckmaster, Prog. Energy Combust. Sci. 28 (2002) 435–475.
[38] B. Cuenot, T.J. Poinsot, Proc. Combust. Inst. 25 (1994) 1383–1390.
[39] S. Mitarai, J.J. Riley, G. Kosály, Phys. Fluids 15 (2003) 3856–3866.
[40] H. Pitsch, C.M. Cha, S. Fedotov, Combust. Theory Model. 7 (2003) 317–332.
[41] S. Mitarai, G. Kosály, J.J. Riley, Combust. Flame 137 (2004) 306–319.
[42] J. Buckmaster, P. Clavin, A. Liñán, M. Matalon, N. Peters, G.I. Sivashinsky, F.A. Williams, Proc. Combust. Inst. 30 (2005) 1–19.
[43] A. Liñán, Acta Astronaut. 1 (1974) 1007–1039.
[44] D.C. Kyritsis, V.S. Santoro, A. Gomez, Proc. Combust. Inst. 29 (2002) 1679–1685.
[45] M. Vera, A. Liñán, Phys. Fluids 16 (2004) 2237–2254.
[46] W.J.A. Dahm, C.M. Scheil, G. Tryggvason, J. Fluid Mech. 205 (1989) 1–43.
[47] D.L. Marcus, J.B. Bell, Phys. Fluids 6 (1994) 1505–1514.
[48] C.H. Gibson, Phys. Fluids 11 (1968) 2305–2315.
[49] J. Daou, A. Liñán, Combust. Theory Model. 2 (1998) 449–477.
[50] C. Pantano, D.I. Pullin, Combust. Flame 137 (2004) 295–305.
[51] E. Fernández-Tarrazo, M. Vera, A. Liñán, Combust. Flame 144 (2006) 261–276.
[52] B. Michaelis, B. Rogg, Combust. Sci. Technol. 177 (2005) 955–978.
[53] C. Pantano, D.I. Pullin, J. Fluid Mech. 480 (2003) 311–332.
[54] Z.B. Lu, S. Ghosal, J. Fluid Mech. 513 (2004) 287–307.
[55] A.R. Kerstein, Proc. Combust. Inst. 29 (2002) 1763–1773.
[56] S.E. Widnall, C.-Y. Tsai, Proc. R. Soc. London 287 (1977) 273–305.
[57] P.G. Saffman, J. Fluid Mech. 84 (1978) 625–639.
[58] M. Hermanns, J.A. Hernández, submitted for publication.
[59] G.L. Pellett, K.M. Isaac, W.M. Humphreys Jr., L.R. Gartrell, W.L. Roberts, C.L. Dancey, G.B. Northam, Combust. Flame 112 (1998) 575–592.